ADVANCED MATERIALS
www.advmat.de

Highly Anisotropic Organometal Halide Perovskite Nanowalls Grown by Glancing-Angle Deposition

Javier Castillo-Seoane, Lidia Contreras-Bernal, Jose Manuel Obrero-Perez, Xabier García-Casas, Francisco Lorenzo-Lázaro, Francisco Javier Aparicio, Carmen Lopez-Santos, Teresa Cristina Rojas, Juan Antonio Anta, Ana Borrás, Ángel Barranco, and Juan Ramon Sanchez-Valencia**

Polarizers are ubiquitous components in current optoelectronic devices as displays or photographic cameras. Yet, control over light polarization is an unsolved challenge, since the main drawback of the existing display technologies is the significant optical losses. In such a context, organometal halide perovskites (OMHP) can play a decisive role given their flexible synthesis with tunable optical properties such as bandgap and photoluminescence, and excellent light emission with a low non-radiative recombination rate. Therefore, along with their outstanding electrical properties have elevated hybrid perovskites as the material of choice in photovoltaics and optoelectronics. Among the different OMHP nanostructures, nanowires and nanorods have lately arisen as key players in the control of light polarization for lighting or detector applications. Herein, the fabrication of highly aligned and anisotropic methylammonium lead iodide perovskite nanowalls by glancing-angle deposition, which is compatible with most substrates, is presented. Their high alignment degree provides the samples with anisotropic optical properties such as light absorption and photoluminescence. Furthermore, their implementation in photovoltaic devices provides them with a polarization-sensitive response. This facile vacuum-based approach embodies a milestone in the development of last-generation polarization-sensitive perovskite-based optoelectronic devices such as lighting appliances or self-powered photodetectors.

1. Introduction

In the last decade, organometal-halide perovskites (OMHPs) have fascinated the research community due to their exceptional optoelectronic properties, finding applications as solar cells,[1,2] light-emitting devices,[3,4] and photodetectors.[5–7] Within these applications, the synthesis by vacuum deposition arises as an industrial scalable, low cost, and environmentally friendly methodology to fabricate efficient, stable, and durable optoelectronic devices.[8–11] Moreover, the anisotropic nanostructuration of OMHP such as nanorods, nanowires, or nanoplatelets has been achieved by different routes,[6,12–14] which can be divided into template- and chemical-assisted growth:[15] the first makes use of template structures such as electrospun fibers[16] or nanostructures such as pillars or grooves[17,18] to grow the OMHP in its interior, while the second, the most used, employs solution synthetic approaches to control the growth such as surfactants or anion-exchange reactions, among others.[12,19] One crucial characteristic of these semiconductor anisotropic nanostructures is their polarization-sensitive optoelectronic response.[15,20–22] Although many of our current devices make use of polarizers to produce polarized light, there are several drawbacks, such as the reduced intensity of the generated beam and/or their integration in micro- and nanoscale devices, limiting the overall efficiency of the optoelectronic systems.[15,23]

J. Castillo-Seoane, L. Contreras-Bernal, J. M. Obrero-Perez, X. García-Casas, F. Lorenzo-Lázaro, F. J. Aparicio, C. Lopez-Santos, T. C. Rojas, A. Borrás, Á. Barranco, J. R. Sanchez-Valencia
Institute of Materials Science of Seville (US-CSIC)
Americo Vespucio 49, Seville 41092, Spain
E-mail: angelbar@icmse.csic.es; jrsanchez@icmse.csic.es

The ORCID identification number(s) for the author(s) of this article can be found under https://doi.org/10.1002/adma.202107739.

DOI: 10.1002/adma.202107739

J. Castillo-Seoane, J. R. Sanchez-Valencia
Atomic, Nuclear and Molecular Physics Department
Facultad de Física
University of Seville
Avd. Reina Mercedes s/n, Seville 41012, Spain

F. J. Aparicio, C. Lopez-Santos
Department of Applied Physics I
University of Seville
Virgen de Africa, Seville 41011, Spain

J. A. Anta
Área de Química Física
Universidad Pablo de Olavide
Seville 41013, Spain

The use of anisotropic OMHP nanostructures is proposed as one of the main candidates for the development of polarized light sources and absorbers due to their outstanding properties, such as facile synthesis, tunable bandgap, narrow emission, and high quantum photoluminescence yield.[12,24] Critically, this application requires the ad hoc alignment of the nanostructures, which is not straightforward in the standardized solution-based synthetic routes. Different strategies can be addressed within the state of the art for the alignment of OMHP[25] but most of them are intrinsically incompatible with the development of devices. For example, in oriented polymeric extruded or electrospun matrices, the handicap is related to the presence of a polymeric phase surrounding the nanostructures; only small areas can be generated in the case of electric-field-assisted alignment; in the template or liquid-crystal-assisted methodologies, both materials need to be compatible with the final device processing. Other techniques like the evaporation-mediated strategy present problems with organometal halide perovskites such as solvent compatibility.[25] These difficulties in the implementation are critical when dealing with large scales, limiting their applications in real optoelectronic devices.[15,23,25]

In this work, we propose the application of an evolved version of the vacuum technique glancing-angle deposition (GLAD)[26–29] as an advanced alternative to the synthesis of anisotropic-supported OMHP nanostructures. GLAD has gained interest and prominence as a tool to tune the nanostructure and compactness of thin films and layers. The tilting of the substrates with respect to a punctual material source imposes a growth mechanism dominated by the geometrical shadowing. This shadowing impedes the deposition in the zones behind the initial nuclei promoting the formation of a nanocolumnar structure, which is usually tilted toward the vapor source of deposition. These nanocolumns are highly separated along the direction of the vapor source, while along the perpendicular direction are associated, this latter effect is known as "bundling".[26–29] The bundling effect provides the direct formation of aligned nanostructures on most possible substrates, including photovoltaic devices.[30] Even though its experimental simplicity, the application of GLAD has already revolutionized the fabrication of tailored porous and sculptured films in topics ranging from energy to biomaterials, including optics and optoelectronics.

Our approach is a two-step fabrication procedure consisting of the room-temperature deposition of PbI_2 at glancing angles, followed by deposition of CH_3NH_3I at normal incidence (0°). Vacuum-sublimated methylammonium lead iodide (MAPI) perovskite layers are usually synthesized by co-evaporation of lead iodide and methylammonium iodide (CH_3NH_3I, MAI) precursors.[9,10] Although some examples can be found in the literature regarding the sequential vacuum evaporation at room temperature of both molecules,[31–33] the relatively compact initial inorganic film hinders the penetration of the methylammonium iodide within the entire bulk crystal to react and form the perovskite. With our methodology, highly porous PbI_2 layers are formed in the first instance, allowing the MAI to react with the entire structure. As a result, highly anisotropic MAPI nanostructures resembling "nanowalls" have been fabricated. Such alignment degree endows the samples with anisotropic optical properties such as UV-visible absorption and photoluminescence (PL). Moreover, their implementation in n–i–p OMHP solar cells can be used to develop self-powered polarization-sensitive photodetectors along the visible range. Therefore, the application of GLAD provides highly anisotropic, microstructure, and thickness-controlled OMHP, with potential for large-area fabrication. This technique is fully compatible with microelectronic and optoelectronic processing methods including complementary metal–oxide–semiconductor and roll-to-roll technologies, opening the path toward the development of tunable anisotropic optoelectronic devices based on OMHPs.

2. Results and Discussion

Scheme 1 details the synthetic protocol applied for the fabrication of the OMHP nanowalls. PbI_2 was sublimated under high vacuum conditions on substrates positioned at normal incidence (0°) and glancing angles and then exposed to MAI precursor as shown in the scheme. **Figure 1** shows the X-ray diffraction (XRD) peaks of PbI_2 normal (0°) deposited sample (red and green curves) and GLAD at 85° (blue and brown) before and after deposition of MAI. Whereas the compact PbI_2 sample deposited at 0° does not show any change after the deposition of the MAI in the XRD spectra (green curve), the glancing-angle-deposited one (at 85°) undergoes an almost complete transformation to $MAPbI_3$ (brown curve), as can be observed by the loss of the main XRD peak at 12.7° corresponding to PbI_2 and appearance of the MAPI (110) one at 14.2°. The peaks associated with every crystalline (*hkl*) plane are highlighted with orange triangles (PbI_2 hexagonal), blue diamonds (PbI_2 hexagonal 6R polytype), and brown squares (MAPI). A high texturization is observed in the diffractogram of MAPI, corresponding to a preferential orientation along the (110) crystalline plane. The GLAD PbI_2 before the exposition of MAI presents a very noisy diffractogram as measured in air. Figure S1 in the Supporting Information shows two XRD diffractograms corresponding to the measurements in air (including a sample encapsulated in poly(methyl methacrylate) within the glovebox), and a third one measured in vacuum, which presents a significantly reduced noise level. For this reason, the diffractogram presented in Figure 1 is the one measured in vacuum, assuring the best preservation of the samples. The PbI_2 GLAD diffractogram presents the main peak at 12.7° and additional minor peaks that correspond to the polytype of PbI_2 6R as reported elsewhere.[34] The reference used for the indexation of the GLAD PbI_2 crystalline planes is shown in Figure S1 in the Supporting Information. Despite the presence of additional peaks, the diffractogram of GLAD PbI_2 shows a preferential texturization along the (003) direction before the exposition of MAI. The full-width at half-maximum (FWHM) of the main XRD peak for GLAD samples, is much higher for PbI_2 (001) (0.79°) than for MAPI (110) (0.18°), indicating that the deposition of MAI (performed over PbI_2 GLAD samples at 50 °C) induces a preferential crystal transformation and growth as reported elsewhere.[35] In addition, the transformation to MAPI is appreciable by the naked eye, since it changes its color from yellow to brown as it is shown in the insets of Figure 1.

Figure 2 shows the top-view scanning electron microscopy (SEM) images at different magnifications of GLAD perovskite

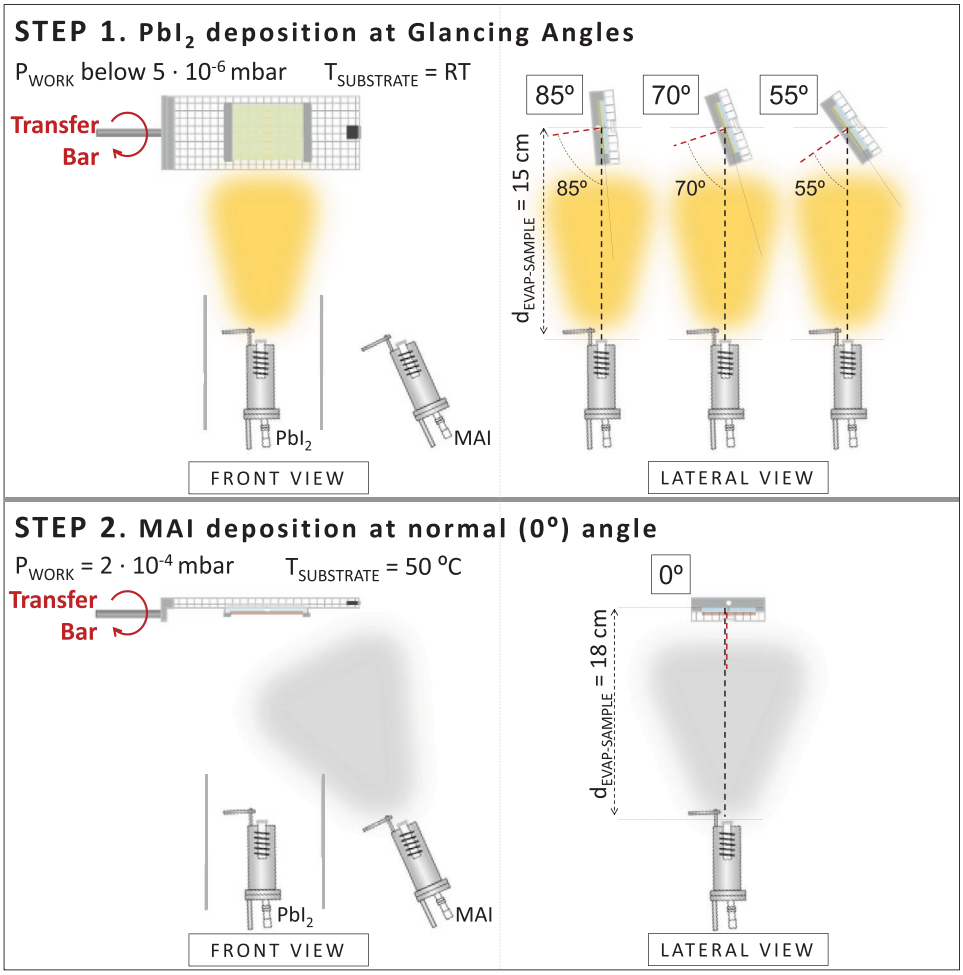

Scheme 1. Two-step sequential GLAD methodology including the relevant experimental parameters. Step 1 (top) schematizes the GLAD of PbI_2 at the different deposition angles tested (85°, 70°, and 55°). Step 2 (bottom) shows the MAI sublimation onto the PbI_2 deposited samples placed at 0° with respect to the evaporation source. Front and lateral views are represented for a comprehensive understanding of the protocol.

thin films deposited at 70° (Figure 2a,b) and 85° (Figure 2c,d) using the detailed two-step sequential protocol. GLAD samples present a highly porous structure that allows the MAI to diffuse within the PbI_2 layer and react to form the MAPI phase, in agreement with the transformation observed in the XRD pattern of Figure 1. It can be noted that the porosity is significantly enhanced for the highest deposition angle of 85°. The high-magnification images of Figure 2b,d show highly oriented nanostructures that resemble nanowalls (NWs) along the *x*-axis, while leaving open void channels along the *y*-direction. A more detailed analysis of the top-view images of samples deposited at 70° and 85°, plus an additional sample deposited at 55° is shown in Figure S2 in the Supporting Information, including a scheme of the dimensions of the nanowalls, length (*l*, dimension along *x*-direction) and width (*w*, along *y*-direction), as well as the interwall distance (ID). A full description of the average values of the relevant dimensions as well as their standard deviation is also shown in Figure S2 in the Supporting Information. It can be noted that while the length and ID increases with the deposition angle ($l = 1.0 \pm 0.5$ and 1.8 ± 0.7 µm and ID = 340 ± 180 and 530 ± 240 nm for 70° and 85°, respectively), the width of the nanowalls decreases ($w = 110 \pm 30$ and 78 ± 23 nm, for 70° and 85°, respectively). This decrease in the width can also be observed in the high-magnification cross-section images gathered in Figure S3 in the Supporting Information.

It is also worth highlighting that the alignment of the NWs increases with the deposition angle. This increased alignment along the *x*-axis can be seen in the fast Fourier transform, FFT, images of top-view SEM pictures shown in Figure S4 in the Supporting Information, that depict a lobe-shape pattern turning narrower as the deposition angle increases. Such a feature is compatible with an increase in the alignment of the MAPI NWs and straightforwardly linked to the shadowing mechanism characteristic of GLAD. Thus, the shadowing effect is enhanced for larger deposition angles. Since the most anisotropic structure is found for the highest deposition angle, we focused the study on this latter case.

The characteristic cross-sectional SEM images of the 85° deposition angle sample are shown in **Figure 3**. As the elongated nanostructures are highly oriented along the *x*-axis, the cross-sectional views are different for samples cleaved along the *y*- or *x*-direction. Figure 3a,b and 3c,d show these different

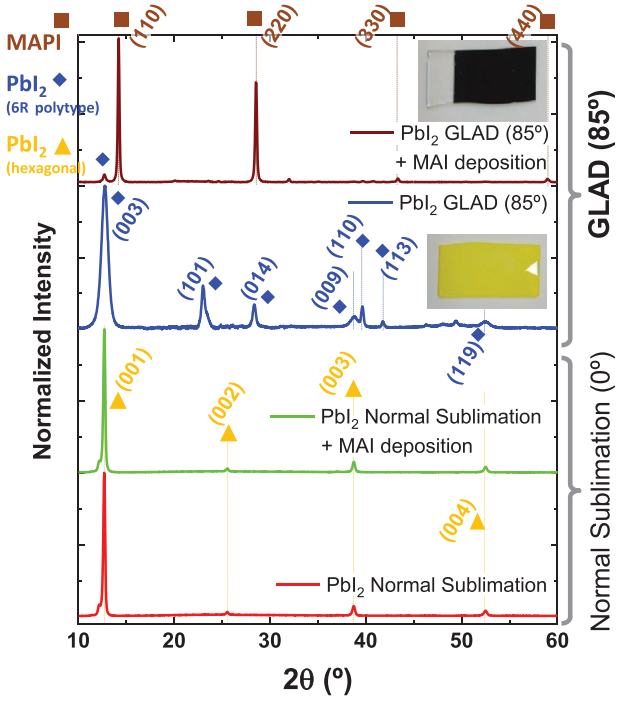

Figure 1. X-ray diffractograms of PbI_2 normal deposited sample (red and green curves) and GLAD at 85° (blue and brown) before (red and blue) and after (green and brown) deposition of MAI. The peaks associated with every crystalline (hkl) plane are indicated with orange triangles (PbI_2), blue diamonds (PbI_2 hexagonal 6R polytype), and brown squares (MAPI). The insets show the corresponding image of PbI_2 GLAD before and after MAI deposition.

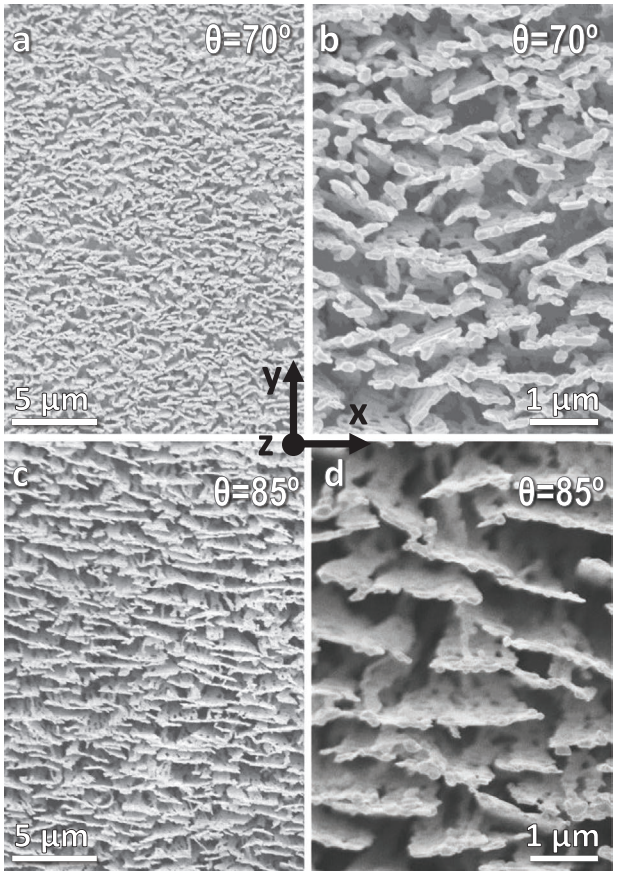

Figure 2. a–d) Top-view SEM images of GLAD perovskite thin films deposited at 70° (a,b) and 85° (c,d) at two different magnifications. The arrows are included to indicate the geometrical axes, where *x* corresponds to the alignment direction.

cuts along the *y*–*z* and *x*–*z* planes, respectively. The microstructure observed in Figure 3a (*y*–*z* plane) consists of apparently 1D nanowires slightly tilted toward the source of PbI_2 vapor during deposition. Contrarily the *x*–*z* plane views show a continuous layer with an apparent lower porosity.

The images confirm the growth of quasi-vertical 2D NWs with a strong orientation along the *x*–*z* plane. The coalescence of the nanostructures along the *x*-direction (perpendicular to the deposition direction) is commonly known as bundling and has been observed in many GLAD systems.[26,28,36,37] Unlike conventional bundling that is usually a nanocolumnar association, the nanostructures observed here present, to the best of our knowledge, the highest anisotropy observed for a GLAD nanostructure.[26]

The transmission electron microscopy (TEM) image of **Figure 4**a shows an overview of transferred perovskite NWs (henceforward 85°), where many fragments (from the transfer procedure, see the Experimental Section) with different sizes and shapes can be identified. Some of these fragments are stacked as it can be deduced from the darker appearance at some locations (highlighted with orange circles). A representative nanowall fragment is presented in Figure 4b. One important observation is the very high sensitivity of the samples to the electron beam that degrades the fragments in a very short time. This effect is shown in Figure 4b,c, where it can be noted how the original single perovskite nanowall (Figure 4b) is degraded after a few seconds under the 200 keV accelerated electron beam (Figure 4c). The inset in Figure 4c is a magnified image of the area marked in red showing the damage induced by beam irradiation. The selected-area electron diffraction (SAED, shown in Figure 4d) pattern obtained from the fragment shown in Figure 4c (green circle) reveals a hexagonal arrangement that could be initially associated with the (111) surface of the tetragonal structure of MAPI. However, a close inspection of the SAED image shown in Figure 4f (obtained from the small fragment of Figure 4e) reveals the transformation of the MAPI to PbI_2, as can be deduced from the distances extracted from the diffraction image. In particular, the pattern observed corresponds to the [001] zone axis of the hexagonal crystal structure of PbI_2 (shown in Figure 4g), where it can identify the periodic distances of 2.2 and 3.9 Å, in good agreement with the (110) and (100) plane spacing.[38] Such damaging effect is typical in hybrid metal halide perovskites as has been previously reported elsewhere and has prompted the development of ad hoc tools to circumvent this issue such as controlling the electron dose over the specimen.[39,40] However, and despite this degradation to PbI_2, the results in Figure 4 allow us to identify a single crystalline growth all along the individual fragments observed. Thus, the SAED images of more than ten ensembles show the same hexagonal arrangement (see Figure S5 in the Supporting Information). These results are consistent with a highly texturized

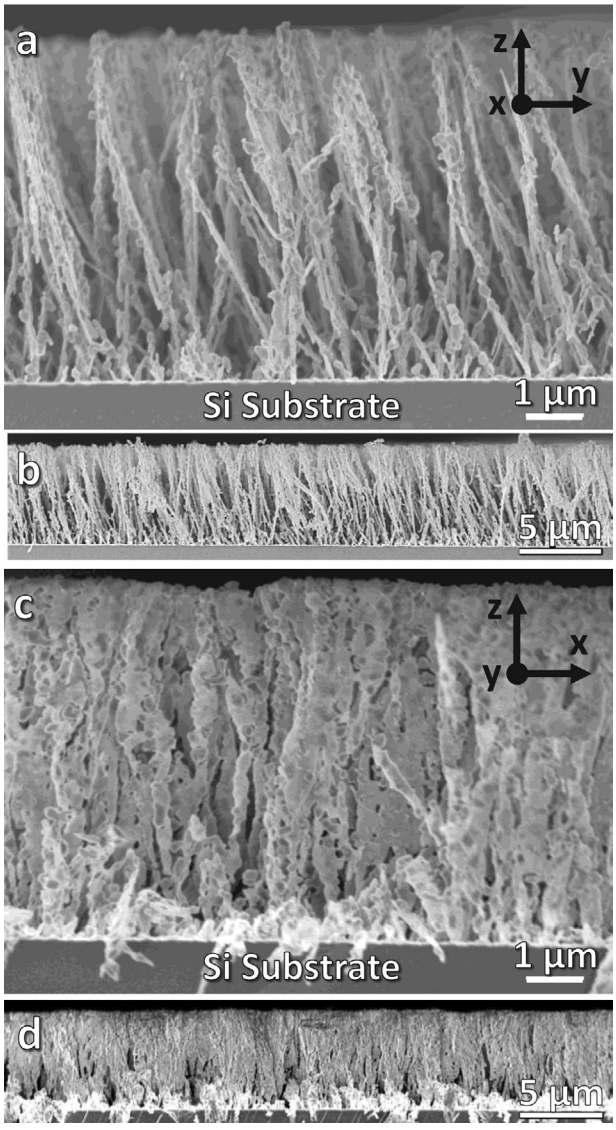

Figure 3. a–d) Cross-sectional SEM images of GLAD perovskite thin films deposited at 85° cleaved along the *y*-direction (*y*–*z* plane) (a,b) and *x*-direction (*x*–*z* plane) (c,d) with different magnifications. The arrows are included to indicate the geometrical axes.

crystalline orientation of the MAPI nanowalls, supported by the strong (003) orientation observed in the XRD pattern of Figure 1. Although many articles have reported the increased or reduced texturization induced by GLAD in systems such as metal, metal oxides, or organic materials,[26,41–43] such a high crystalline orientation is yet outstanding.

As a direct consequence of the perovskite nanowalls alignment, the samples show anisotropic optical properties. It is worth stressing herein that the proposed methodology allows a fine thickness control by simply increasing the deposition time without detriment in the composition homogeneity, being such one of the additional advantages over the chemical- and template-assisted approaches. Hence, since the 6 μm thickness samples shown in Figures 2 and 3 present an almost complete absorption in the UV–vis range for both polarizations, a sample with 2 µm thickness was used for the optical studies of **Figure 5**. Figure 5a shows the ultraviolet–visible–near infrared (UV–vis–NIR) absorptance spectra using polarized light beams along the *x*- and *y*-directions (see the Experimental Section), being the *x*-axis the alignment direction of the nanowalls as presented in Figure 2c,d of the sample deposited at 85°. To avoid degradation, the samples were measured in an inert atmosphere inside a homemade airtight sealing packing between two fused silica windows (see the Experimental Section and Figure S6, Supporting Information). The direct and total transmittance (T_{Dir} and T_T), the total reflectance (R_T), and the calculated absorptance (A, also shown in Figure 5a) for the 2 µm thickness MAPI NWs sample are shown in Figure S7a–d in the Supporting Information. The highly diffuse component of the transmittance can be noted, especially along *x*-polarization where the direct transmittance is around zero. Thus, the optical properties further corroborate the transformation from PbI_2 to MAPI. This can be noted in the Tauc plots shown in Figure S8 in the Supporting Information, where a bandgap of 1.617 eV for both polarizations can be extracted. Although this value is slightly above the expected value for MAPI (1.59–1.60 eV),[44] it is consistent with the nanostructuration of the developed NWs.[45] On the other side, Figure 5b presents the absorptance difference between *x*- and *y*-polarization and demonstrates the anisotropy shown in these samples, with a visible difference in the light absorptance between the two in-plane polarizations. It can be observed that the absorptance difference presents positive/negative values above/below 620 nm and is almost zero for wavelengths above 770 nm. The absorptance difference is negative and relatively flat around 4–6% in a relatively broad range from 250 to 550 nm, and positive (around 4–6%) in a much narrower range (670–770 nm).

The PL of the MAPI-aligned nanowalls for both polarizations is shown in Figure 5c, revealing a blueshift with respect to that expected for the bulk MAPI, which is also consistent with the nanostructuration of the NWs (see also Figure S8, Supporting Information to compare the absorptance with the PL bands for both polarizations).[45] Interestingly, the PL reveals very strong anisotropic properties, showing a much more intense PL emission polarized along the *x*-axis when excited with unpolarized light at 600 nm. It is remarkable that the different intensities of the PL for both excitation polarizations are obtained by illuminating at 600 nm, where the absorptance difference is nearly zero (see Figure 5b). Such a feature demonstrates that the different polarized light absorption is not responsible for the PL anisotropy. Figure 5d–f shows the polar diagram of the PL emission (illuminating with unpolarized excitation light) and excitation polarization (recording unpolarized emission light), using different excitation wavelengths, 400 (Figure 5d), 500 (Figure 5e), and 600 nm (Figure 5f). First, it can be noted that both the anisotropy in the emission (black line) and excitation polarization (colored line) increase with wavelength. The case of excitation at 600 nm (Figure 5f) shows the typical lobe-shape pattern for both PL excitation and emission polarization. For shorter excitation wavelengths, the excitation polarization is nearly isotropic with a quasi-circular shape. By contrast, the emission polarization retains the lobe-shape pattern for all the wavelengths studied, with a continuous reduction in the anisotropy as the wavelength decreases.

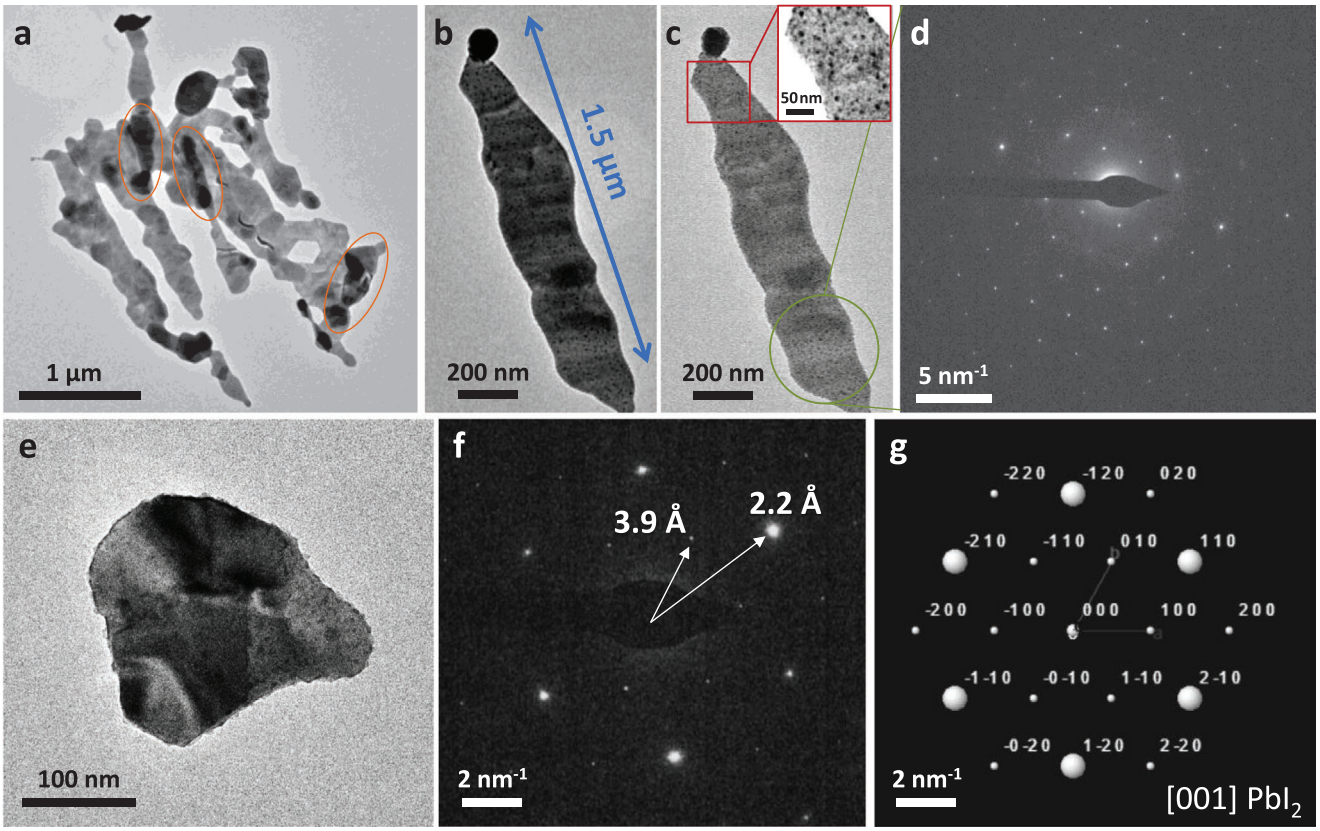

Figure 4. a) Overview of the transferred samples. Stacked layers are highlighted with orange circles. b,c) TEM images of individual fragments of MAPI NWs at short exposure to the e-beam (b) and after a few seconds (c). The inset in (c) shows a magnified image of the highlighted area. d) SAED of the green circle zone in (c). e) MAPI fragment and f) corresponding SAED. g) Simulated diffraction pattern for the [001] axis zone of PbI_2.

From the PL polar representation obtained by exciting at 400 (Figure 5d) and 500 nm (Figure 5e), it can be noted that while the polarization ratio, P, (see Note S1, Electrostatic Approximation, in the Supporting Information) for excitation polarization is very low (P_{EX} = 0.09 for both illumination wavelengths), the emission polarization is significantly higher, P_{EM} = 0.24 and 0.38 for 400 and 500 nm excitation wavelengths, respectively. This difference is consistent with the results reported by Täuber et al., which characterize the PL excitation and emission polarization of individual MAPI nanowires, using a 488 nm laser as the excitation source.[46] They observed a systematic difference between these excitation and emission polarization measurements for 28 different isolated nanocrystals at room temperature, with a much lower P_{EX} value, in agreement with our measurements using a similar excitation wavelength (Figure 5e). Moreover, in the cited work[46] the maximum P_{EM} for 28 individual nanocrystals is 0.37 while in our case is 0.38 for a macroscopic sample (probed over ≈1 cm^2), i.e., the average all over our aligned anisotropic nanowalls. This value is highly remarkable, and one of the highest obtained for MAPI anisotropic nanostructures.[22,46] Furthermore, the P_{EM} is even higher as the excitation wavelength increases, reaching 0.43 for excitation at 600 nm, closer to the bandgap of MAPI. These results could be initially attributed to the dielectric constant contrast between MAPI and the surrounding environment as detailed in Note S1 in the Supporting Information, which should result in a polarization ratio of P = 0.92. Although some authors have used this approximation for perovskite anisotropic nanostructures such as $MAPbBr_3$[22,47] or $CsPbBr_3$[48,49] with a certain agreement, the detailed study of individual MAPI nanowires[46] revealed that this approximation is not correct due to the strong differences observed in the excitation and emission polarization measurements, as observed here. This difference is attributed in literature to the orientation of the crystalline nanostructure: the room-temperature tetragonal structure is noncentrosymmetric and consequently the bond angles and lengths between Pb^{2+} and I^- differ for the two dissimilar planes (namely, the equatorial and apical planes), producing modifications in the bandgap due to the hybridization of the 6s orbitals of lead and the 5p of iodide.[46] The smaller energy bandgap arises for the apical direction where the bond angles are smaller and possesses a transition dipole moment that results in a polarized PL. Consequently, it can be assumed that for polycrystalline ensembles, this effect is negligible. Surprisingly, these authors observed an isotropic behavior in the excitation polarization by using excitation sources with energy well above the bandgap and foresaw a nonisotropic behavior for lower energies, although it was not measured. This is the exact phenomenon that also accounted for our MAPI nanowalls and the first evidence that supports their hypothesis.[46] This result is also in agreement with the high texturization observed by XRD and TEM, indicating a preferential crystalline orientation all along the nanowalls.

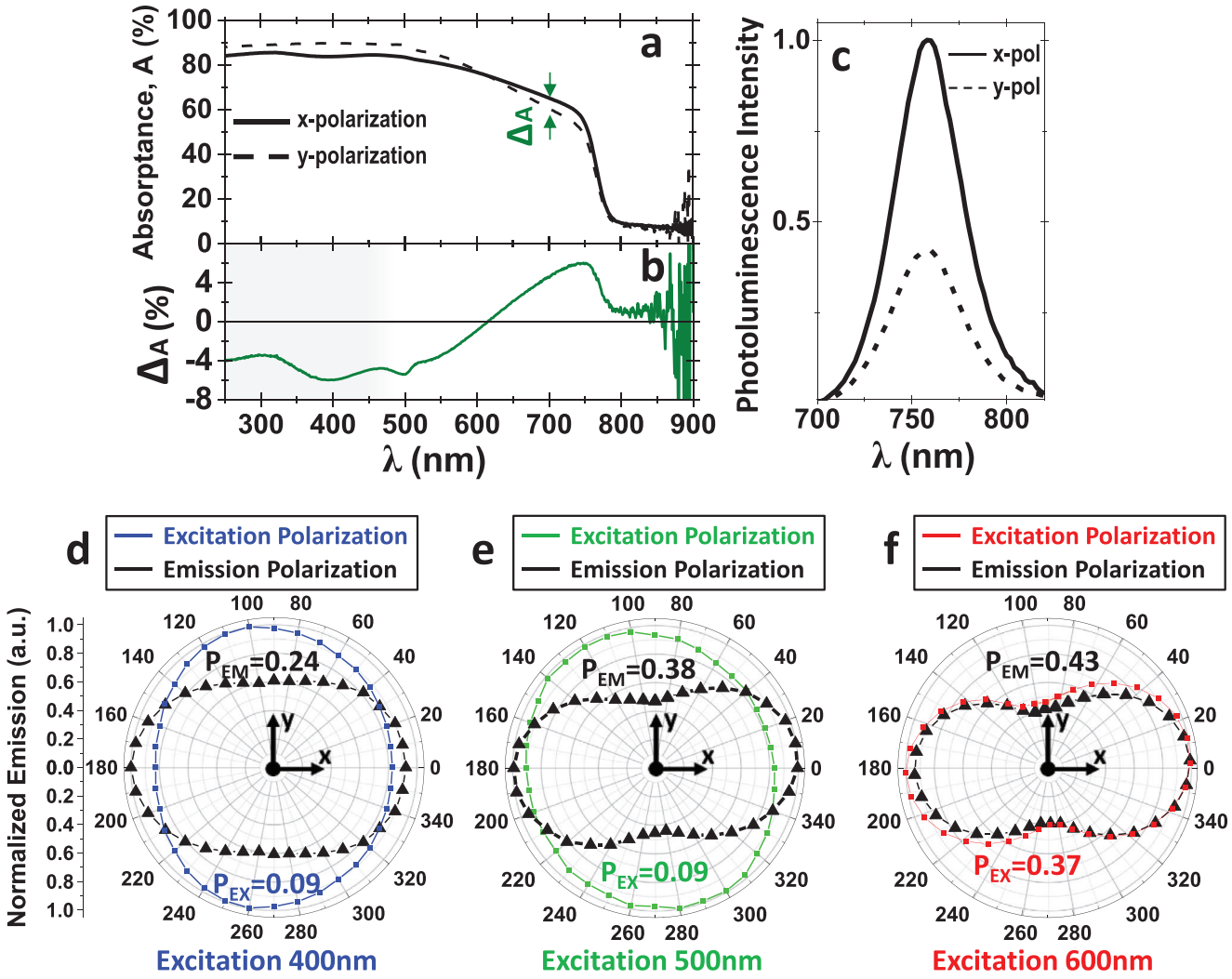

Figure 5. a) UV–vis–NIR absorptance spectra of MAPI NWs using polarized light along *x*- (solid line) and *y*-polarization (dashed line) and b) absorptance difference ($\Delta_A = A(x\text{-pol}) - A(y\text{-pol})$). c) Photoluminescence emission polarized spectra along the *x*- (solid line) and *y*-polarization (dashed line) exciting with unpolarized light at 600 nm. d–f) Azimuthal polar representation of the PL emission polarization (using unpolarized excitation light, black line) and excitation polarization (recording unpolarized emission light, colored line), using 400 nm (d), 500 nm (e), and 600 nm (f) as excitation wavelengths.

As introduced above, the advantage of our approach is its granted full compatibility with the deposition over an ample variety of substrates. Figure S9 in the Supporting Information shows the deposition of MAPI NWs on different substrates with increasing roughness levels from TiO_2 thin film (the same used for the photodetector shown below), indium tin oxide deposited on a poly(ethylene terephthalate) (PET), aluminum foil to copper adhesive tape. Although aligned MAPI NWs have been grown over all the substrates tested, it needs to be taken into account that for rough surfaces like Al foil and Cu adhesive tape, the microstructure obtained is slightly different, increasing the width of the nanowalls from around 80 nm (on Si wafer) to 150 and 200 nm, respectively. This behavior is consistent with the shadowing mechanism detailed above which is enhanced for rough surfaces, especially for higher angles of deposition. As a proof of concept, our MAPI NWs were implemented in an n–i–p solar cell (see the Experimental Section) with thicknesses of 350 and 500 nm to ensure a complete covering of the nanowalls by Spiro-OMeTAD films. **Figure 6**a presents a cross-sectional SEM image of the device integrating MAPI nanowalls of 500 nm thickness, demonstrating their complete coverage. An additional thickness of 700 nm is also included, although it was verified that the tips of the nanowalls were not covered by Spiro-OMeTAD (see Figure S10 in the Supporting Information).

As the MAPI NWs present strong anisotropic properties, the solar cell developed here can be used as a self-powered polarization photodetector. Figure 6b–d show the photocurrent increment of the different samples illuminated with *x*- and *y*-polarized light using the complete spectrum of the solar simulator (Figure 6b) and blocking the illumination spectrum below 500 (Figure 6c) and 700 nm (Figure 6d) employing long-pass filters. To better observe the response, the illumination of the devices was periodically changed from *x*- to *y*-polarization every 10 s (as indicated in the graph with the gray background). In Figure 6b, it can be noted that the device with 350 nm of

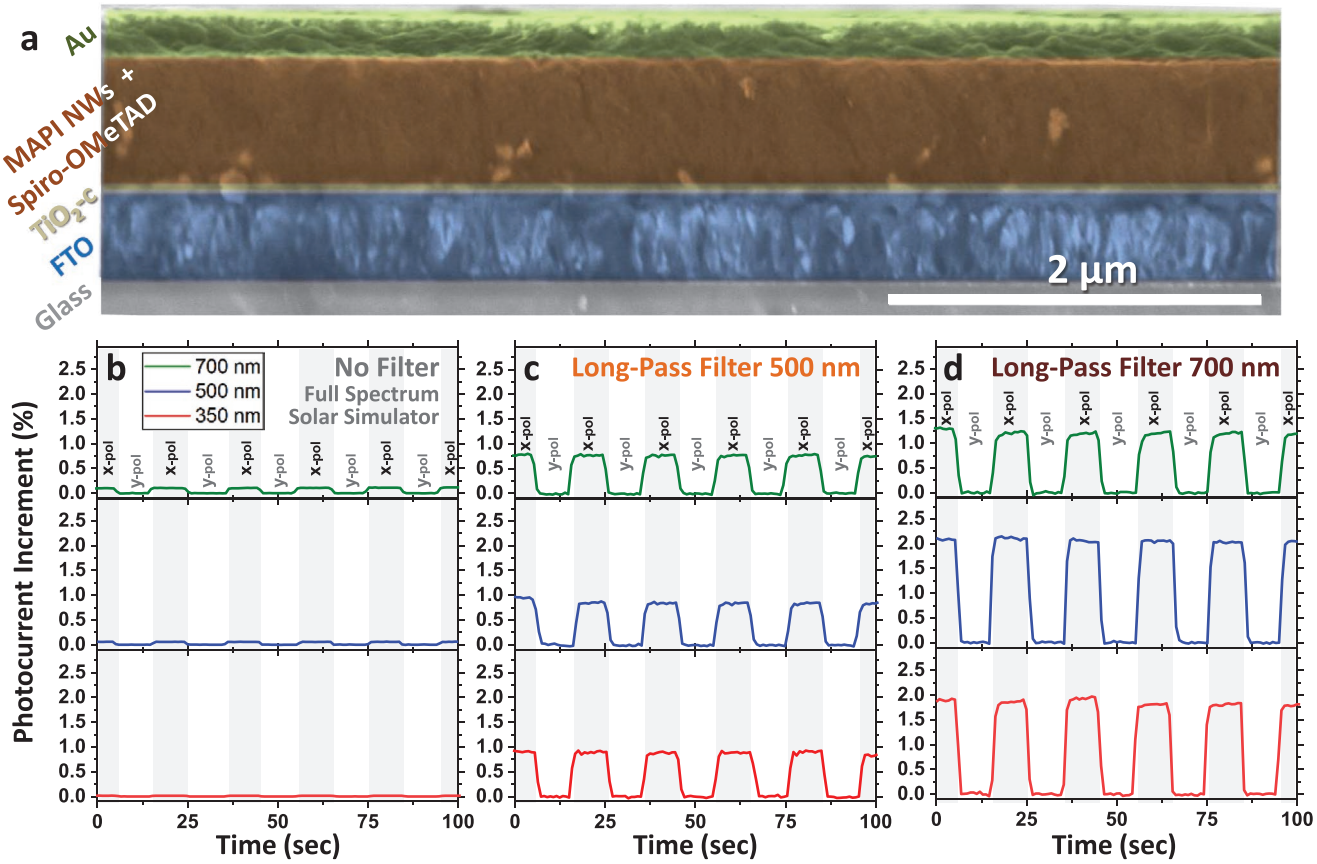

Figure 6. a) Cross-sectional SEM image of the complete solar cell, implementing the MAPI NWs with 500 nm thickness. b–d) Photocurrent increment response recorded by changing between *x*- (higher photocurrents) and *y*-polarization (lower photocurrent) every 10 s for devices implementing MAPI NWs of 350 (red), 500 (blue), and 700 nm (green) thickness. The gray background indicates illumination periods with *x*-polarized light as indicated. The device was tested under illumination with the full solar spectrum (b) and through long pass filters at 500 nm (c) and 700 nm (d).

MAPI (red line) does not show any significant dependence on the polarization. However, the MAPI nanowalls with 500 (blue) and 700 nm (green) thickness depict a certain photocurrent increase with polarized light, which is ≈0.05% and 0.1%. It is worth mentioning that this change is very fast (below the 500 ms used as sampling frequency) for all the cases with a visible response. On the other hand, the illumination through the 500 nm long-pass filter (Figure 6c) produces a significantly higher polarization response, with a maximum photocurrent increase of ≈0.9% for the devices containing nanowalls of 350 and 500 thickness. Furthermore, the illumination with the long-pass filter at 700 nm (Figure 6d), produces similar responses but significantly enhanced, reaching a maximum of 2.1% of photocurrent increase for the device with 500 nm thickness. It can be noted that although the maximum photocurrent anisotropy is expected for the 700 nm sample, the NWs were not completely covered by the Spiro-OMeTAD layer and we observed a much faster degradation, which can also contribute to the reduction in the anisotropy observed.

As a first approximation, the anisotropic response could be related to the absorptance difference between *x*- and *y*-polarization. However, in the case of 700 nm MAPI NWs this difference is very small before and after covering with Spiro-OMeTAD as can be seen in Figures S7 and S11 in the Supporting Information. Additionally, by means of the 500 nm long-pass filter and even more with the 700 nm one, the polarization response is maximized. However, the absorptance difference stands very small, below 4% above 700 nm (red and blue curves in Figure S10 in the Supporting Information, corresponding to the 700 nm thickness sample before and after deposition of Spiro-OMeTAD), indicating a different mechanism for the anisotropic photocurrent response. As it happened with the PL excitation polarization of Figure 5d–f, the anisotropic response is lost for wavelengths below 600 nm and consequently, the visible range where the excitation with polarized light contributes to the anisotropic photocurrents is expected to be redshifted. Thus, our results support even further the previous hypothesis about the crystalline-related anisotropy and show the highly texturized growth of aligned MAPI nanostructures with strong anisotropic properties and their implementation in real devices such as the self-powered polarization photodetector presented.

3. Conclusions

We have shown the synthesis of methylammonium lead iodide perovskite nanostructures by GLAD, producing highly

anisotropic nanowalls. At the highest angle tested, 85°, highly aligned nanowalls along one single axis (*x*-direction) of around 2–4 µm length and widths below 100 nm were formed. XRD analysis reveals a high crystalline texturization along (110) plane for MAPI NWs, in agreement with the hexagonal arrangement observed in the SAED pattern and indicating that the approach can be used to direct the crystalline growth of MAPI. Such nanostructures present the highest anisotropy generated by GLAD.[26] Concretely, in-plane optical anisotropy, with a visible absorptance difference for polarized light along/perpendicular to the NW axis. Moreover, the PL shows a wavelength-dependent anisotropic response with strong differences in the emission (using unpolarized excitation) and excitation polarization (using unpolarized emission). While the excitation at shorter wavelengths produces a nearly isotropic excitation polarization, the excitation at 600 nm yields a typical anisotropic lobe-shape pattern. At the same time, the emission polarization is anisotropic for all the wavelengths studied and has been quantified with the polarization ratio which magnitude increases with wavelength and reaches values as high as 0.43. This result marks a milestone in the state of the art, especially taking into account that only isolated nanorods have so far provided values close to this, and here we have a macroscopic sample composed of aligned individual anisotropic nanowalls. As proof of concept, the MAPI nanowalls were implemented in a solar cell used as a self-powered polarization photodetector. The excitation with polarized light produces different photocurrents, being higher for the direction of the nanowalls (with a 2.1% photocurrent increase between *x*- and *y*-polarization).

The responses of the NWs against the excitation with polarized light, i.e., the PL excitation and photocurrent polarization, have been related to their crystalline orientation and confirm not only the results of the literature regarding PL of individual MAPI nanowires, but also with their predictions with respect to their wavelength-dependent response.[46] We have demonstrated here the potential application of GLAD for the synthesis of highly anisotropic OMHP nanostructures with many operational advantages: i) direct integration and alignment degree of the NWs in virtually any substrate; ii) environmental friendly methodology since it is a solventless process at low temperature; and iii) compatibility with industrially scalable processes. It is worth mentioning that the generality of our methodology will allow the synthesis of other OMHP, for instance, with PL and photocurrent responses shifted to the visible by just tilting the substrates. For these reasons, we believe that our results will increase the potential of the development of full vacuum-processed polarization-sensitive optoelectronic devices and pave the way for future developments based on the nanostructuring of supported OMHP.

4. Experimental Section

Sequential GLAD of MAPI: Lead Iodide (PbI_2) and methylammonium iodide (MAI) were acquired from TCI and used as received. Both precursors were sublimated by means of two separated Knudsen cells and heated up to temperatures around 330 and 160 °C for PbI_2 and MAI, respectively. Scheme 1 shows a description of the experimental set-up and the two steps methodology for the growth of MAPI NWs. The evaporator to sample distance was 15 cm (18 cm in the case of MAI evaporator due to the tilting angle shown in the front view of Scheme 1). The initial PbI_2 deposition was carried out at pressures below 5×10^{-6} mbar on fused silica and Si(100) wafer pieces. The deposition was also performed over fluorine-doped tin oxide (FTO) commercial pieces as detailed in the next subsection. The substrates were positioned at oblique and glancing angles of 55°, 70°, and 85° with respect to the evaporation source as indicated in Step 1 of Scheme 1 (lateral view). The rotation of the samples was performed employing a transfer bar that allowed both the angle control by the use of a goniometer and to transfer them into a glovebox. The deposition rate was controlled using a quartz crystal monitor (QCM) located at the same height as the samples with a constant growth rate of 1.5 nm s^{-1}. After this, the MAI was sublimated onto the PbI_2 deposited samples placed at 0° with respect to the evaporation source (Step 2 in Scheme 1). This was performed with the samples at a constant temperature of 50 °C. It was observed that the deposition of MAI could not be properly controlled by the QCM as referenced in the literature.[50] The initial growth rate achieved during the first minutes could not be maintained for the whole deposition, and the MAI was finished before the complete transformation to MAPI. It was also noted that different from the PbI_2 deposition, the MAI sublimation produced an increase in the pressure of the system. Based on these observations and according to the literature,[50] an optimization process was proceeded and reproducible and stable conditions were found by maintaining the evaporation temperature of the MAI precursors at 160 °C, which produced an increase in the pressure to around $(5–8) \times 10^{-5}$ mbar. Then, the pumping flux of the turbomolecular pump was reduced using a butterfly valve and fixing the pressure to 2×10^{-4} mbar. With this protocol, reproducible MAPI NWs samples were obtained.

Photodetector Multilayer: MAPI NWs-containing devices were fabricated on FTO glasses (TEC 15 Pilkington, resistance 15 Ω $square^{-1}$, 82–84.5% visible transmittance) patterned by laser etching supplied by XOP glass. FTOs were cleaned by ultrasonic bath following the solvent sequence: 1) Hellmanex water solution (2:98 vol/vol ratio); 2) deionized water; 3) isopropyl alcohol; 4) acetone. An UV ozone treatment for 15 min was done as a final cleaning step. After that, 50 nm of compact TiO_2 was deposited on top of the FTO substrates by spray pyrolysis. The sprayed solution comprised 1 mL of titanium diisopropoxide bis(acetylacetonate) solution (75% in 2-propanol, Sigma-Aldrich) and 14 mL of absolute ethanol. The solution was sprayed on heated substrates (450 °C) using pure oxygen as a carrying gas. The samples were kept at 450 °C for 30 min for the formation of the TiO_2 anatase phase. The compact TiO_2 layer was doped with lithium. For that, a lithium solution precursor was prepared with 10 mg of bis(trifluoromethane)sulfonimide lithium salt (Sigma-Aldrich) in 1 mL of acetonitrile (Across Organics). Then, this solution was spin coated on compact layer at 3000 rpm and 2000 rpm s^{-1} for 10 s. The samples were quickly annealed again at 450 °C for 30 min (using reported temperature ramp).[51] Once the electrodes were cooled down, these were moved into a glovebox to deposit a thin (30 nm) methylammonium lead iodide (MAPI) perovskite layer. First, a MAPI precursor solution was obtained using dimethylformamide (DMF, Acros) as solvent in which, first, dimethyl sulfoxide (DMSO, Acros), then PbI_2 (heated up to 70 °C without stirring), and finally, MAI (at room temperature) were dissolved. The concentration of the three compounds, DMSO, PbI_2, and MAI, was 1.3 M. Finally, this precursor solution was diluted (1:4 vol%) using a DMF:DMSO solvent-mix (9:1 vol%). Then, MAPI film was deposited on lithium-doped TiO_2 substrate by spin-coating following a reported one-step protocol: 5000 rpm for 50 s. 6 s after the beginning of the spinning, the DMF was selectively washed with nonpolar diethyl ether (Sigma-Aldrich). Afterward, the samples were annealed at 65 °C for 1 min and then for 2 min at 100 °C. On top of these samples, sequential glancing-angle-deposited MAPI NWs were synthesized, except for the reference photodetector samples. The samples were transferred to the vacuum system with the aid of a transfer bar and a gate valve coupled to the glovebox. After the deposition of the MAPI NWs, the samples were transferred again to the glovebox (without exposing them to the air), and Spiro-OMeTAD was spin coated on top of them in a two-step protocol: 1) 500 rpm for 20 s; 2) 1000 rpm for 10 s. The hole transport material solution was obtained from 72.3 mg of Spiro-OMeTAD (Merck) dissolved

in 1 mL of chlorobenzene (Acros). The Spiro-OMeTAD solution was doped with 6.6 µL of a *tris*(2-(1*H*-pyrazol-1-yl)-4-*tert*-butylpyridine)cobalt(III) (FK209, Sigma-Aldrich) stock solution (400 mg in 1 mL of acetonitrile), 14.5 µL of tri[bis(trifluoromethane)sulfonimide]lithium salt (LiTFSI) stock solution (520 mg of LiTFSI in 1 mL of acetonitrile), and 26 µL of 4-*tert*-butylpyridine (tBP, Sigma-Aldrich). Finally, 60 nm of gold was deposited by thermal evaporation under vacuum at pressures between 1×10^{-6} and 1×10^{-5} mbar on a water-cooled sample holder at a growth rate of 0.1 Å s^{-1} for the first 20 nm and then 1 Å s^{-1}.

Characterization of Films and Photodetector: SEM images were acquired in a Hitachi S5800, provided with a field emission gun and using electrons accelerated to 2 kV. The samples were deposited on Si(100) wafers that allowed a correct cleavage to observe the cross-section images. The samples were mounted on the SEM sample-holder inside the glovebox and packed in inert atmosphere for their transportation to the microscope. After that, the samples were exposed to the atmosphere a few seconds for their transfer to the SEM.

TEM images and SAED pattern were obtained using a scanning TEM microscope, TALOS F200S from FEI company, working at 200 kV with 0.25 nm resolution. To perform these measurements, the samples were scratched on top of a holey carbon TEM copper grid. This procedure was performed inside a glovebox and the grids were packed under inert atmosphere for their transportation. The grids were exposed to air for a very short time during their positioning on the TEM sample holder. The program EjeZ from the University of Cadiz[52] was used to simulate the digital diffraction patterns.

Optical characterization was performed in a spectrophotometer model Perkin-Elmer Lambda 750 UV/vis/NIR. For the total transmittance and reflectance (T_T and R_T, respectively), the samples were positioned at the input and output, respectively, of an integrating sphere coupled to the spectrophotometer. The absorptance, A, was calculated by the formula $A = 1 - T_T - R_T$. The spectra were acquired in the range 250–900 nm as a function of the polarization using a Glan–Taylor polarizer positioned along the optical path of the light beam. The absorption coefficient, α, of the samples was calculated with the following relation[53]

$$\alpha = -\left(\frac{1}{d}\right) \ln\left[\frac{T_T}{(1-R_T)^2}\right] \quad (1)$$

where d is the thickness of the sample. The Tauc plots were used to calculate the bandgap of the MAPI samples. As the MAPI is a direct-bandgap semiconductor, for the calculation $(\alpha E)^2$ versus E (where E is the energy of the light beam) was represented.

PL spectra were recorded in a Jobin Yvon Fluorolog-3 spectrofluorometer using the front face configuration. The equipment was provided with two automated polarizers after the excitation and emission monochromators, respectively. To correct the polarization dependence of the detector with the polarization of the light, a MAPI layer prepared by solution was used as an isotropic emitter. To avoid degradation, samples were sealed in an inert atmosphere inside a homemade packing for both measurements, optical and photoluminescence. The sample was located between two fused silica windows that were previously glued to a polymeric bag with two apertures to allow the optical measurements. This homemade airtight sealing bag was evacuated with a pump that reached around 600 mbar and was thermally sealed inside the glovebox. Some representative pictures and schemes of the homemade airtight compartment are shown in Figure S6 in the Supporting Information.

For structural characterization, X-ray diffractograms were acquired in a Panalytical X'PERT PRO instrument in the Bragg–Brentano configuration using the Cu K_α (1.5418 Å) radiation as the excitation source. For the glancing-angle-deposited PbI_2, a controlled atmosphere cell was used and measured under vacuum.

Short-circuit current curves versus time were measured under a solar simulator (ABET-Sun2000) with an AM 1.5G filter. The samples were measured in a closed holder under N_2 atmosphere. A depolarizer provided by Varian was used to reduce the partial polarization of the solar simulator. After this, a Glan–Taylor polarizer (Varian) was used that was periodically rotated from 0° to 90° every 10 s and below, a long pass filter of 500 and 700 nm was provided by Edmund-Optics. The reference sample, which was consisted of a thin layer of MAPI synthesized by spin coating, also shows a certain dependence on the illumination polarization. This effect, attributed to the partial polarization of the light source (the solar simulator), could not be suppressed employing a depolarizer. To correct the photocurrent increment of the samples with respect to the reference, the curves were initially normalized (from 0 to 1) and subtracted a baseline. After that, the contribution to the photocurrent increment of the reference samples was subtracted to the MAPI NWs containing photodetectors.

Supporting Information

Supporting Information is available from the Wiley Online Library or from the author.

Acknowledgements

The authors thank the projects PID2019-110430GB-C21, PID2019-110430GB-C22 and PID2019-109603RA-I00 funded by MCIN/AEI/10.13039/501100011033 and by "ERDF (FEDER) A way of making Europe", by the "European Union". They also thank the Consejería de Economía, Conocimiento, Empresas y Universidad de la Junta de Andalucía (PAIDI-2020 through projects US-1263142, US-1381045, US-1381057, AT17-6079, P18-RT-3480), and the EU through cohesion fund and FEDER 2014–2020 programs for financial support. C.L.S. and J.S.-V. thank the University of Seville through the VI PPIT-US. J.S.-V. and C.L.S. acknowledge the "Ramon y Cajal" and L.C.-B the "Juan de la Cierva" programs funded by MCIN/AEI/ 10.13039/501100011033. F.J.A. also thanks the EMERGIA Junta de Andalucía program. The projects leading to this article have received funding from the EU H2020 program under the grant agreements 851929 (ERC Starting Grant 3DScavengers). J.A.A. thanks MCIN/AEI/ 10.13039/501100011033 for SCALEUP SOLAR-ERA.net project PCI2019-111839-2. The authors also thank the laboratory of materials characterization INMALAB of Universidad Pablo de Olavide for experiments and technical support.

Conflict of Interest

The authors declare no conflict of interest.

Data Availability Statement

Research data are not shared.

Keywords

anisotropic nanostructures, organometal-halide perovskites, photoluminescence polarization, self-powered polarization photodetectors

Received: September 27, 2021
Revised: December 23, 2021
Published online: March 14, 2022

[1] J. Y. Kim, J.-W. Lee, H. S. Jung, H. Shin, N.-G. Park, *Chem. Rev.* **2020**, *120*, 7867.
[2] M. A. Green, E. D. Dunlop, J. Hohl-Ebinger, M. Yoshita, N. Kopidakis, A. W. Y. Ho-Baillie, *Prog. Photovoltaics* **2020**, *28*, 3.

[3] X.-K. Liu, W. Xu, S. Bai, Y. Jin, J. Wang, R. H. Friend, F. Gao, *Nat. Mater.* **2021**, *20*, 10.
[4] L. Chouhan, S. Ghimire, C. Subrahmanyam, T. Miyasaka, V. Biju, *Chem. Soc. Rev.* **2020**, *49*, 2869.
[5] M. Long, P. Wang, H. Fang, W. Hu, *Adv. Funct. Mater.* **2019**, *29*, 1803807.
[6] H.-P. Wang, S. Li, X. Liu, Z. Shi, X. Fang, J.-H. He, *Adv. Mater.* **2021**, *33*, 2003309.
[7] F. P. García de Arquer, A. Armin, P. Meredith, E. H. Sargent, *Nat. Rev. Mater.* **2017**, *2*, 16100.
[8] A. Barranco, M. C. Lopez-Santos, J. Idigoras, F. J. Aparicio, J. Obrero-Perez, V. Lopez-Flores, L. Contreras-Bernal, V. Rico, J. Ferrer, J. P. Espinos, A. Borras, J. A. Anta, J. R. Sanchez-Valencia, *Adv. Energy Mater.* **2020**, *10*, 1901524.
[9] J. Ávila, C. Momblona, P. P. Boix, M. Sessolo, H. J. Bolink, *Joule* **2017**, *1*, 431.
[10] S. Bhaumik, M. R. Kar, B. N. Thorat, A. Bruno, S. G. Mhaisalkar, *ChemPlusChem* **2021**, *86*, 558.
[11] J. Idígoras, F. J. Aparicio, L. Contreras-Bernal, S. Ramos-Terrón, M. Alcaire, J. R. Sánchez-Valencia, A. Borras, Á. Barranco, J. A. Anta, *ACS Appl. Mater. Interfaces* **2018**, *10*, 11587.
[12] A. R. bin M Yusoff, M. K. Nazeeruddin, *Adv. Energy Mater.* **2018**, *8*, 1702073.
[13] X. Zhang, S. Chen, X. Wang, A. Pan, *Small Methods* **2019**, *3*, 1800294.
[14] C. Zhang, J. Chen, S. Wang, L. Kong, S. W. Lewis, X. Yang, A. L. Rogach, G. Jia, *Adv. Mater.* **2020**, *32*, 2002736.
[15] Y. Ge, L. Meng, Z. Bai, H. Zhong, *J. Inf. Disp.* **2019**, *20*, 181.
[16] J. Xue, T. Wu, Y. Dai, Y. Xia, *Chem. Rev.* **2019**, *119*, 5298.
[17] J. Wang, S. Luo, Y. Lin, Y. Chen, Y. Deng, Z. Li, K. Meng, G. Chen, T. Huang, S. Xiao, H. Huang, C. Zhou, L. Ding, J. He, J. Huang, Y. Yuan, *Nat. Commun.* **2020**, *11*, 582.
[18] P. Liu, X. He, J. Ren, Q. Liao, J. Yao, H. Fu, *ACS Nano* **2017**, *11*, 5766.
[19] J.-K. Sun, S. Huang, X.-Z. Liu, Q. Xu, Q.-H. Zhang, W.-J. Jiang, D.-J. Xue, J.-C. Xu, J.-Y. Ma, J. Ding, Q.-Q. Ge, L. Gu, X.-H. Fang, H.-Z. Zhong, J.-S. Hu, L.-J. Wan, *J. Am. Chem. Soc.* **2018**, *140*, 11705.
[20] L. Zhang, S. Cui, Q. Guo, C. Ge, Q. Han, Q. Lin, C. Li, X. Zheng, Z. Zhai, L. Wang, Q. Sun, Y. Xu, Y. Liu, X. Tao, *ACS Appl. Mater. Interfaces* **2020**, *12*, 51616.
[21] Y. Wei, Y. Xu, Q. Wang, J. Wang, H. Lu, J. Zhu, *Chem. Commun.* **2020**, *56*, 5413.
[22] C.-H. Lin, C.-Y. Kang, T.-Z. Wu, C.-L. Tsai, C.-W. Sher, X. Guan, P.-T. Lee, T. Wu, C.-H. Ho, H.-C. Kuo, J.-H. He, *Adv. Funct. Mater.* **2020**, *30*, 1909275.
[23] C. Fang, M. Xu, J. Ma, J. Wang, L. Jin, M. Xu, D. Li, *Nano Lett.*. **2020**, *20*, 2339.
[24] G. Xing, N. Mathews, S. S. Lim, N. Yantara, X. Liu, D. Sabba, M. Grätzel, S. Mhaisalkar, T. C. Sum, *Nat. Mater.* **2014**, *13*, 476.
[25] A. K. Srivastava, W. Zhang, J. Schneider, J. E. Halpert, A. L. Rogach, *Adv. Sci.* **2019**, *6*, 1901345.
[26] A. Barranco, A. Borras, A. R. Gonzalez-Elipe, A. Palmero, *Prog. Mater. Sci.* **2016**, *76*, 59.
[27] M. M. Hawkeye, M. T. Taschuk, M. J. Brett, *Glancing Angle Deposition of Thin Films: Engineering the Nanoscale*, John Wiley & Sons, New York **2014**.
[28] J. R. Sanchez-Valencia, R. Longtin, M. D. Rossell, P. Gröning, *ACS Appl. Mater. Interfaces* **2016**, *8*, 8686.
[29] Y. Oulad-Zian, J. R. Sanchez-Valencia, M. Oliva, J. Parra-Barranco, M. Alcaire, F. J. Aparicio, A. Mora-Boza, J. P. Espinos, F. Yubero, A. R. Gonzalez-Elipe, A. Barranco, A. Borras, *Adv. Opt. Mater.* **2016**, *4*, 1124.
[30] L. González-García, I. González-Valls, M. Lira-Cantu, A. Barranco, A. R. González-Elipe, *Energy Environ. Sci.* **2011**, *4*, 3426.
[31] M. Á. Reinoso, C. A. Otálora, G. Gordillo, *Materials* **2019**, *12*, 1394.
[32] T. M. Brenner, Y. Rakita, Y. Orr, E. Klein, I. Feldman, M. Elbaum, D. Cahen, G. Hodes, *Chem. Mater.* **2016**, *28*, 6501.
[33] J. Wang, D. Lin, T. Zhang, M. Long, T. Shi, K. Chen, Z. Liang, J. Xu, W. Xie, P. Liu, *CrystEngComm* **2019**, *21*, 736.
[34] P. A. Beckmann, *Cryst. Res. Technol.* **2010**, *45*, 455.
[35] A. Ummadisingu, M. Grätzel, *Sci. Adv.* **2018**, *4*, e1701402.
[36] J. R. Sanchez-Valencia, J. Toudert, A. Borras, A. Barranco, R. Lahoz, G. F. de la Fuente, F. Frutos, A. R. Gonzalez-Elipe, *Adv. Mater.* **2011**, *23*, 848.
[37] J. R. Sánchez-Valencia, J. Toudert, A. Borras, C. López-Santos, A. Barranco, I. O. Feliu, A. R. González-Elipe, *Plasmonics* **2010**, *5*, 241.
[38] Q. Fan, J. Huang, N. Dong, S. Hong, C. Yan, Y. Liu, J. Qiu, J. Wang, Z. Sun, *ACS Photonics* **2019**, *6*, 1051.
[39] K. Song, L. Liu, D. Zhang, M. P. Hautzinger, S. Jin, Y. Han, *Adv. Energy Mater.* **2020**, *10*, 1904006.
[40] D. Johnstone, P. Midgley, *Microsc. Microanal.* **2020**, *26*, 1732.
[41] L. Chen, T.-M. Lu, G.-C. Wang, *J. Appl. Phys.* **2012**, *112*, 024303.
[42] P. Basnet, G. K. Larsen, R. P. Jadeja, Y.-C. Hung, Y. Zhao, *ACS Appl. Mater. Interfaces* **2013**, *5*, 2085.
[43] M. T. Taschuk, M. M. Hawkeye, M. J. Brett, in *Handbook of Deposition Technologies for Films and Coatings* (Ed: P. M. Martin), Elsevier, Oxford, UK **2010**, pp. 621–678.
[44] T. S. Sherkar, C. Momblona, L. Gil-Escrig, J. Ávila, M. Sessolo, H. J. Bolink, L. J. A. Koster, *ACS Energy Lett.* **2017**, *2*, 1214.
[45] Y. Sun, Y. Yin, M. Pols, J. Zhong, Z. Huang, B. Liu, J. Liu, W. Wang, H. Xie, G. Zhan, Z. Zhou, W. Zhang, P. Wang, C. Zha, X. Jiang, Y. Ruan, C. Zhu, G. Brocks, X. Wang, L. Wang, J. Wang, S. Tao, W. Huang, *Adv. Mater.* **2020**, *32*, 2002392.
[46] D. Täuber, A. Dobrovolsky, R. Camacho, I. G. Scheblykin, *Nano Lett.* **2016**, *16*, 5087.
[47] L. Meng, C. Yang, J. Meng, Y. Wang, Y. Ge, Z. Shao, G. Zhang, A. L. Rogach, H. Zhong, *Nano Res.* **2019**, *12*, 1411.
[48] Y. Gao, L. Zhao, Q. Shang, Y. Zhong, Z. Liu, J. Chen, Z. Zhang, J. Shi, W. Du, Y. Zhang, S. Chen, P. Gao, X. Liu, X. Wang, Q. Zhang, *Adv. Mater.* **2018**, *30*, 1801805.
[49] S. N. Raja, Y. Bekenstein, M. A. Koc, S. Fischer, D. Zhang, L. Lin, R. O. Ritchie, P. Yang, A. P. Alivisatos, *ACS Appl. Mater. Interfaces* **2016**, *8*, 35523.
[50] K. L. Heinze, O. Dolynchuk, T. Burwig, J. Vaghani, R. Scheer, P. Pistor, *Sci. Rep.* **2021**, *11*, 15299.
[51] M. Saliba, J.-P. Correa-Baena, C. M. Wolff, M. Stolterfoht, N. Phung, S. Albrecht, D. Neher, A. Abate, *Chem. Mater.* **2018**, *30*, 4193.
[52] J. A. P. Omil, *Ph.D. Thesis*, Universidad de Cádiz, Cádiz, Spain **1995**.
[53] D. C. Look, J. H. Leach, *J. Vac. Sci. Technol. B* **2016**, *34*, 04J105.